Supplementary material for:

"Facile synthesis of molten-salt promoted and hetero-element doped Li_4SiO_4 particles for efficient and stable CO_2 capture"

Yunlian Liu[1, 2], Mingkai Liu[1], Ruqi Zhang[1, 2], Lizhuang Dou[1, 2], Zihan Wan[1, 2], Qian Jia[1,2], Ying Pan[1*], Hongguang Jin[1]

[1] Institute of Engineering Thermophysics, Chinese Academy of Sciences, Beijing 100190, China

[2] University of Chinese Academy of Sciences, Beijing 100049, China

* To whom correspondence should be addressed.

E-mail address: panying@iet.cn

Contents

S1 Material synthesis

Tabel S1. Source of precursor materials.

Reagents Name	Chemical formula	Quality index	Reagent purity	Supplier
Lithium carbonate	Li_2CO_3	Analytical pure	99.8%	Aladdin
Silicon dioxide	SiO_2	Analytical pure	99.5%	Aladdin
Potassium carbonate	K_2CO_3	Analytical pure	99.9%	Aladdin
Aluminum oxide	nano γ-Al_2O_3	Analytical pure	50 nm, 99.99%	Macklin
Titanium dioxide	nano TiO_2	Analytical pure	30 nm, rutile, 99.95%	Aladdin
Iron oxide	nano α-Fe_2O_3	Analytical pure	30 nm, 99.95%	Aladdin
Cerium dioxide	nano CeO_2	Analytical pure	99.8%	Aladdin
Deionized water	H_2O	one-level	≥18MΩ·cm	-

Table S2 Precursor compositions and mass loadings of the K-Li_4SiO_4-based sorbents.

Sample	Precursor molar and mass ratios	Total precursor mass and mass fraction of the (Ti, Al, Fe, Ce)-oxides
K-Li_4SiO_4	n (Li: Si: K) =4.1: 1: 0.2 m (Li_2CO_3: SiO_2: K_2CO_3: cellulose fiber) = 25.2: 10: 2.3 :3.8	Total precursor mass: 41.3g
K-$Li_4Si_{0.95}Ti_{0.05}O_4$	n (Li: Si: Ti: K) =4.1:0.95:0.05:0.2 m (Li_2CO_3: SiO_2: TiO_2: K_2CO_3: cellulose fiber) = 26.5: 10: 0.7 :2.4 :4.0	Total precursor mass:43.6 g Mass fraction of TiO_2: 1.6 wt%

K-$Li_{4.05}Si_{0.95}Al_{0.05}O_4$	n (Li: Si: Ti: K) =4.15:0.95:0.05:0.2 m (Li_2CO_3: SiO_2: Al_2O_3: K_2CO_3: cellulose fiber) = 26.9: 10: 0.5 :2.4 :4.0	Total precursor mass:43.7 g Mass fraction of Al_2O_3: 1.0 wt%
K-$Li_{4.05}Si_{0.95}Fe_{0.05}O_4$	n (Li: Si: Ti: K) =4.15:0.95:0.05:0.2 m (Li_2CO_3: SiO_2: Fe_2O_3: K_2CO_3: cellulose fiber) = 26.9: 10: 0.7 :2.4 :4.0	Total precursor mass:44.0 g Mass fraction of Fe_2O_3: 1.6 wt%
K-$Li_4Si_{0.95}Ce_{0.05}O_4$	n (Li: Si: Ti: K) =4.1:0.95:0.05:0.2 m (Li_2CO_3: SiO_2: CeO_2: K_2CO_3: cellulose fiber) = 26.5: 10: 1.5 :2.4 :4.0	Total precursor mass:44.5 g Mass fraction of CeO_2: 3.4 wt%

S2 Characterization methods

Characterization methods

The structural, morphological, and surface properties of the sorbents were systematically characterized to elucidate their CO_2 capture behavior. Phase composition and crystallite size were determined by X-ray diffraction (XRD) on a Bruker D8 Advance (Cu Kα radiation, λ = 1.5406 Å) operated at 40 kV and 40 mA, with 2θ scanned from 10° to 90°. Microstructural features and dopant distribution were examined via scanning electron microscopy coupled with energy-dispersive X-ray spectroscopy (SEM–EDS) using a Zeiss Gemini 300 microscope equipped with an Oxford X-MaxN detector. N_2 adsorption-desorption isotherms were measured at -196 °C on a Micromeritics ASAP 2020; specific surface areas were calculated by the Brunauer-Emmett-Teller (BET) method, while pore-size distributions and volumes were derived using the Barrett-Joyner-Halenda (BJH) model. Raman spectra were acquired at room temperature using a Horiba LabRAM Odyssey Raman spectrometer equipped with a 532 nm laser; the instrument was calibrated using a silicon wafer standard. Finally, the mechanical robustness of the particles was assessed through uniaxial compressive strength tests conducted on a Siwei Shanghai testing machine, with each sample measured at least ten times to obtain statistically reliable average values.

S3 N_2 adsorption results of Li_4SiO_4 sorbent powders

Table S3. N_2 adsorption results of K-Li_4SiO_4-based sorbent powders with different doping elements.

Sorbent	BET surface area (m^2/g)	Pore volume (cm^3/g)	Pore Size (nm)
K-Li_4SiO_4	3.3	2.9×10^{-2}	17.6
K-$Li_4Si_{0.95}Ti_{0.05}O_4$	3.8	3.2×10^{-2}	18.3
K-$Li_4Si_{0.95}Al_{0.05}O_4$	3.7	3.2×10^{-2}	19.7
K-$Li_4Si_{0.95}Fe_{0.05}O_4$	3.5	3.1×10^{-2}	16.7
K-$Li_4Si_{0.95}Ce_{0.05}O_4$	3.4	3.0×10^{-2}	17.1

S4 SEM-EDS images of Li_4SiO_4 sorbent powders

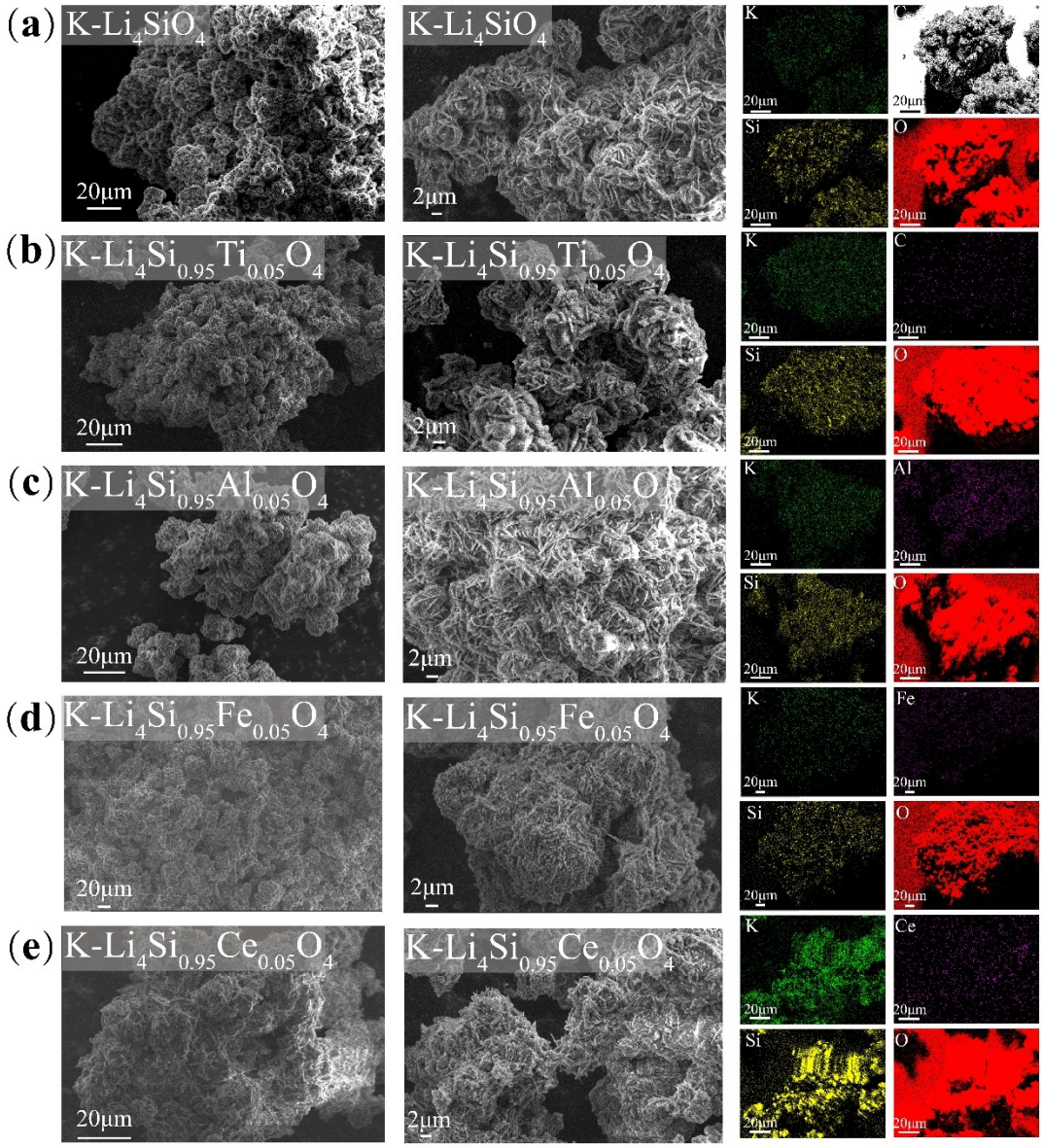

Fig. S1. SEM-EDS images of Li_4SiO_4 sorbent powders with different doping elements.

S5 Cyclic sorption-desorption curves of Li_4SiO_4-based sorbent powders

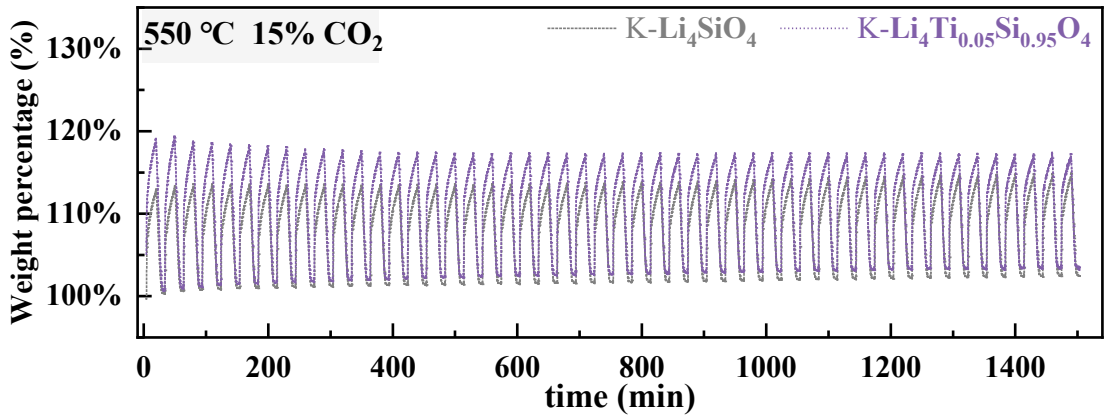

Fig. S2. 50 cyclic sorption-desorption curves of K-Li_4SiO_4 and K-$Li_4Si_{0.95}Ti_{0.05}O_4$ powder at 550°C.

S6 XRD patterns of Li_4SiO_4-based sorbent

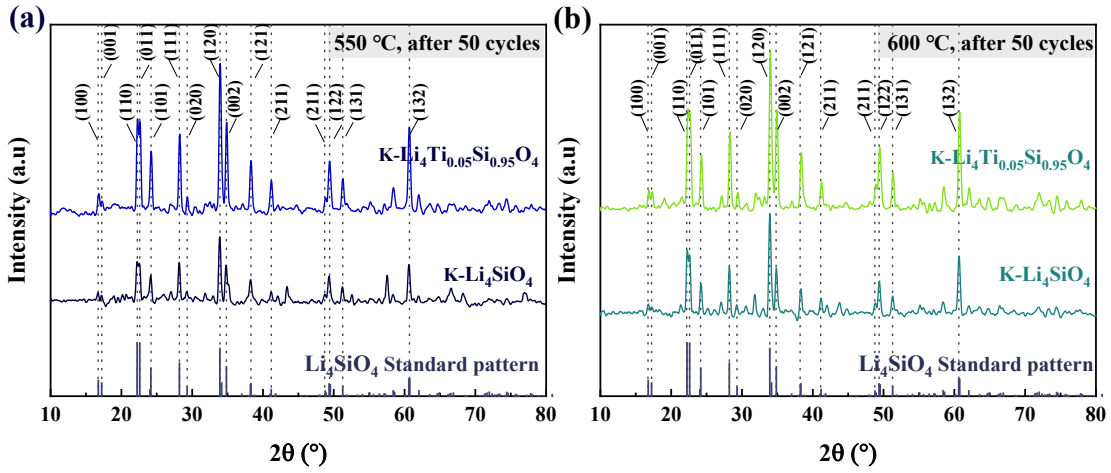

Fig. S3. XRD patterns of K-$Li_4Si_{0.95}Ti_{0.05}O_4$ and Li_4SiO_4 sorbent powders after 50 sorption-desorption cycles at different temperatures. (a) 600°C, (b) 550°C.

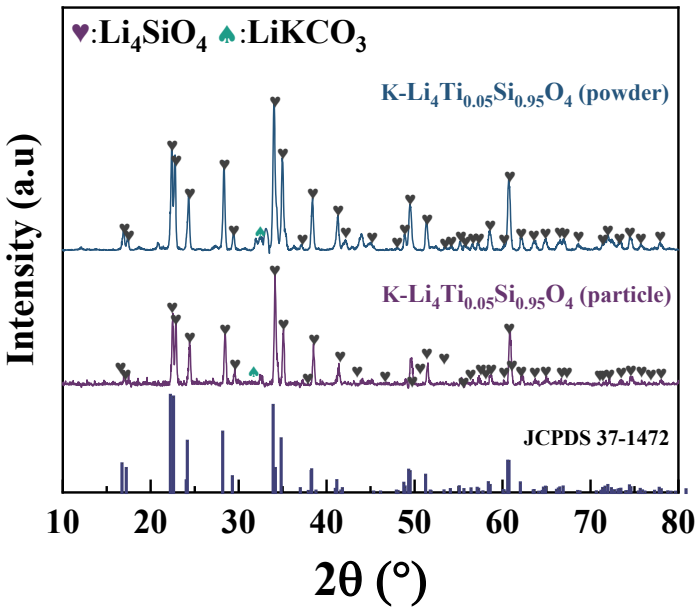

Fig. S4 Comparison of XRD patterns for K-$Li_4Si_{0.95}Ti_{0.05}O_4$ in powder and particle forms.

S7 Effect of calcination temperature and duration

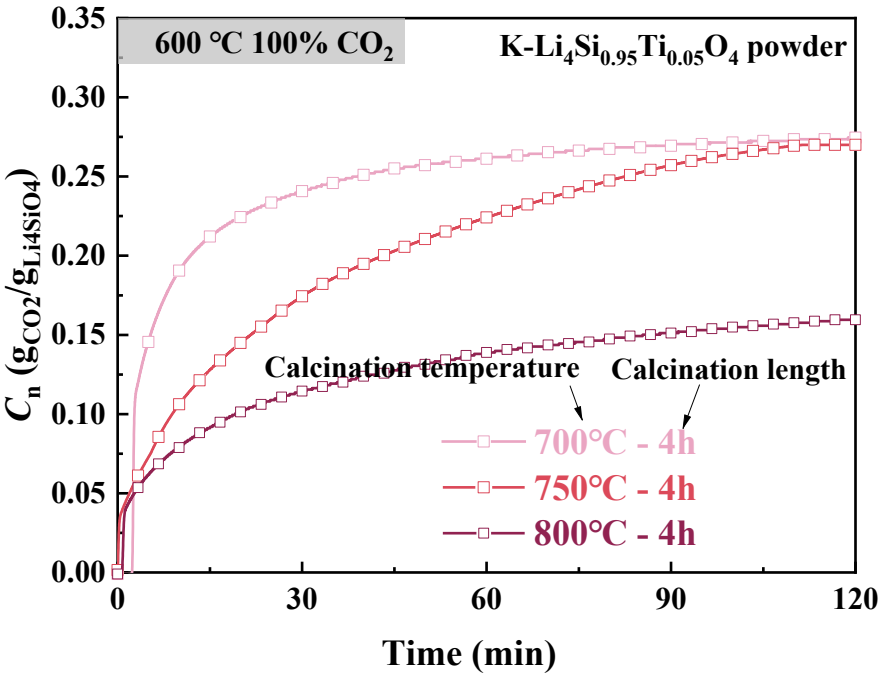

Fig. S5 CO_2 sorption performance of K-$Li_4Si_{0.95}Ti_{0.05}O_4$ sorbent powders calcined at 700–800 °C for 4 h

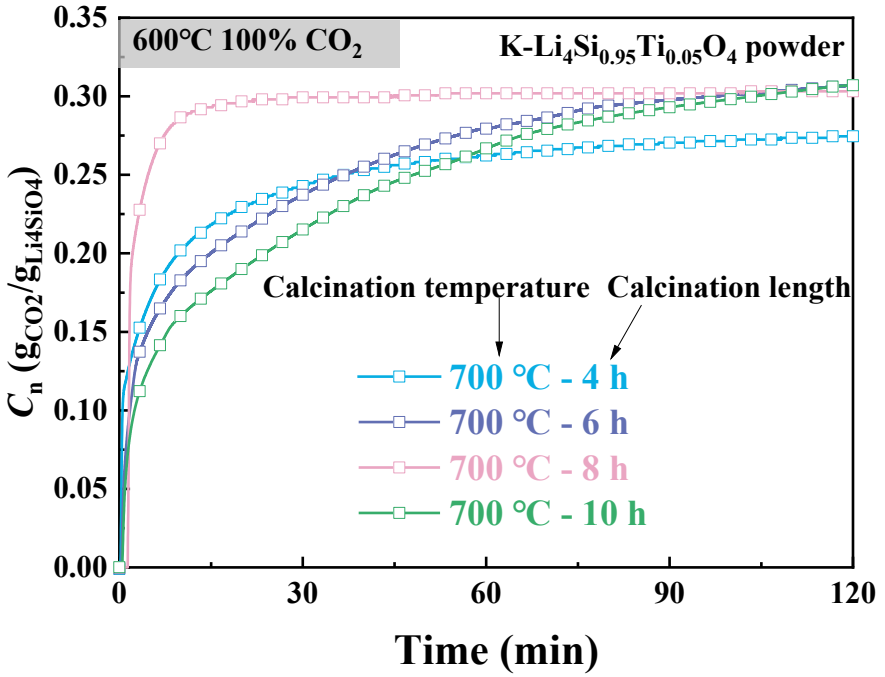

Fig. S6 CO_2 sorption performance of K-$Li_4Si_{0.95}Ti_{0.05}O_4$ sorbent powders calcined at 700 °C for 4–10 h

Table S4. Physical properties of fresh K-$Li_4Si_{0.95}Ti_{0.05}O_4$ and K-Li_4SiO_4 sorbent powders.

Sorbent	Calcination temperature (°C)	Calcination time (h)	BET surface area (m^2/g)	Pore volume (cm^3/g)	Pore Size (nm)
K-Li_4SiO_4	700	8	3.5	3.1×10^{-2}	16.7
K-$Li_4Si_{0.95}Ti_{0.05}O_4$	700	4	2.6	2.8×10^{-2}	21.6
		6	3.1	4.4×10^{-2}	28.1
		8	3.8	3.2×10^{-2}	18.3
		10	2.3	2.9×10^{-2}	23.6
	750	4	2.0	2.9×10^{-2}	28.3
	800	4	0.5	4.5×10^{-3}	36.1

S8 Porosity analysis of Li_4SiO_4-based sorbent

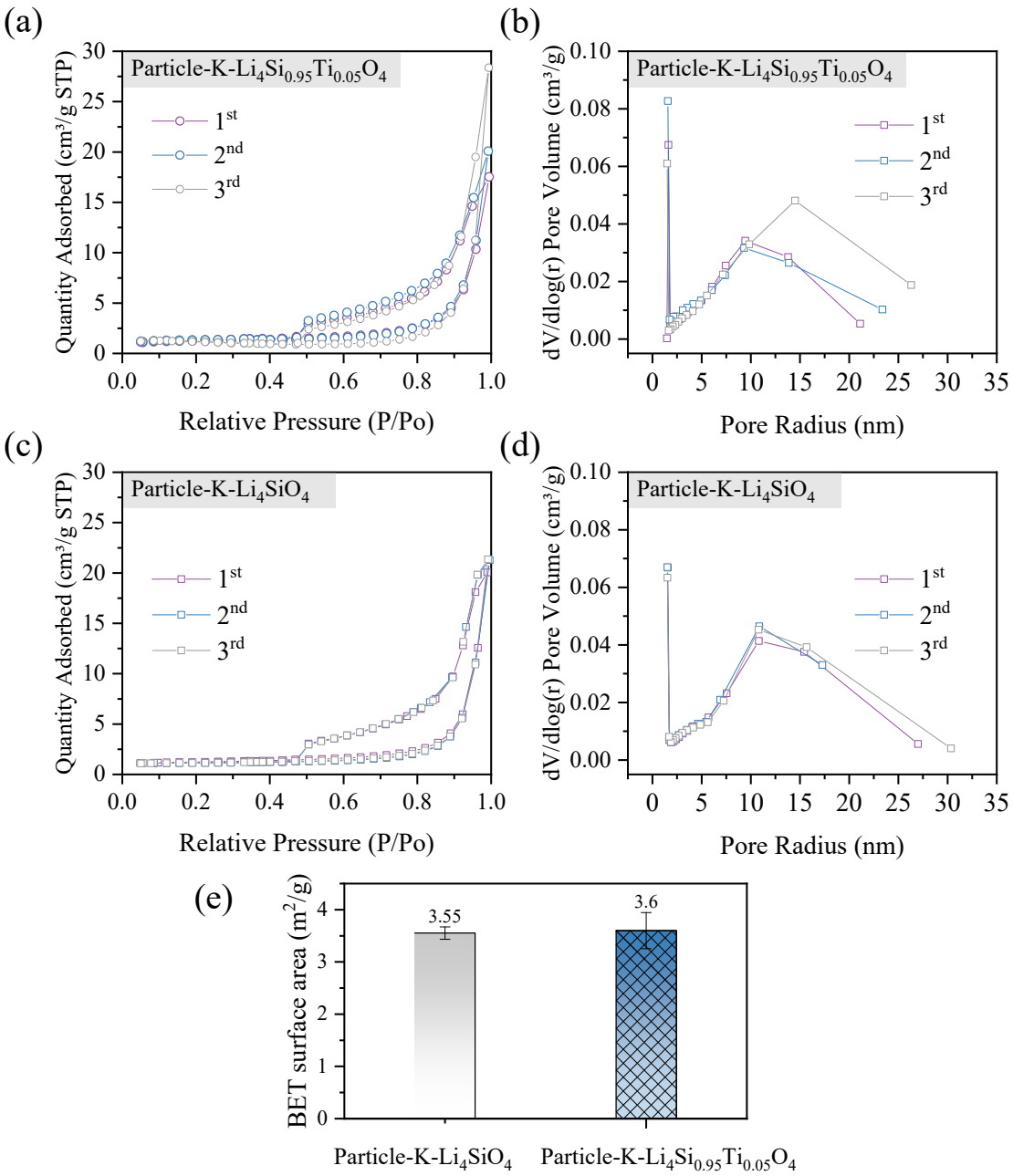

Fig. S7. N_2 adsorption–desorption isotherms (left) and corresponding BJH pore size distribution curves (right) of (a, b) K-$Li_4Si_{0.95}Ti_{0.05}O_4$ particles and (c, d) K-Li_4SiO_4 particles. (e) BET surface area of K-$Li_4Si_{0.95}Ti_{0.05}O_4$ and K-Li_4SiO_4 particles.

S9 Element mappings of fresh K-$Li_4Si_{0.95}Ti_{0.05}O_4$ particle

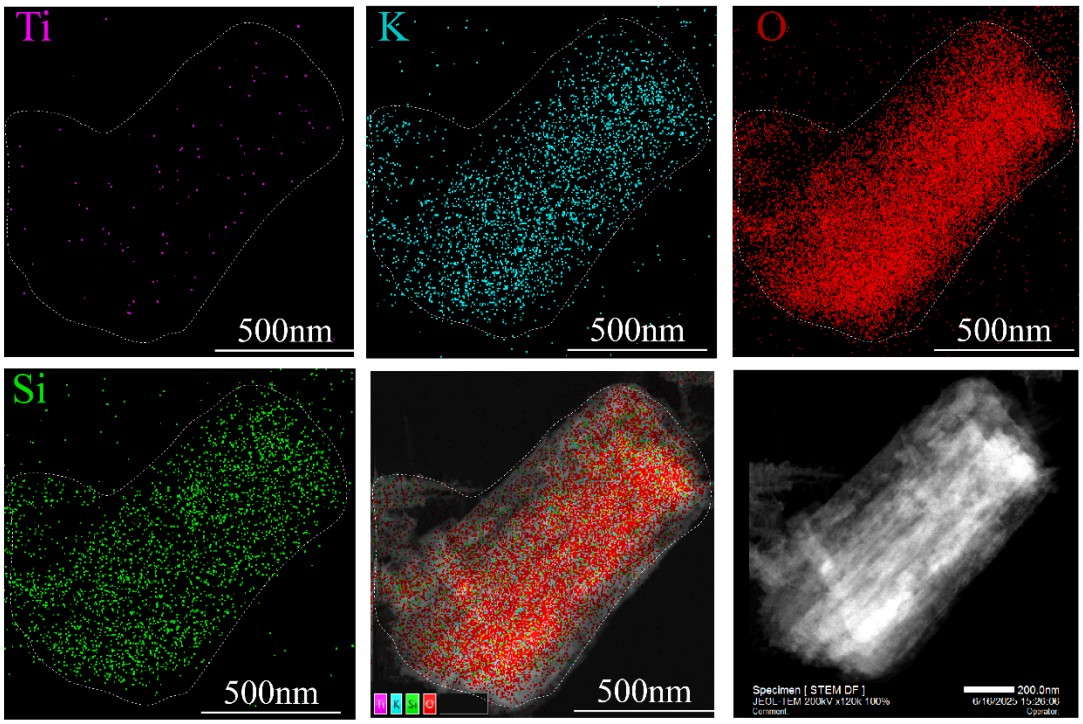

Fig. S8. Scanning Transmission Electron Microscopy (STEM) image and element mappings of fresh K-$Li_4Si_{0.95}Ti_{0.05}O_4$ particle.

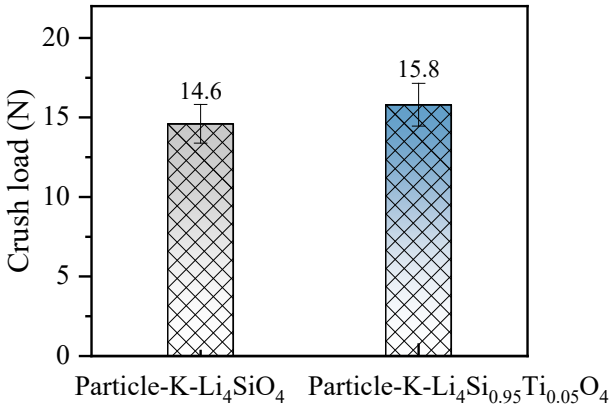

Fig. S9 Compressive strength of the K-Li_4SiO_4 and K-$Li_4Si_{0.95}Ti_{0.05}O_4$ particles after 100 cycles.

S10 Desorption performance in CO_2-rich atmospheres

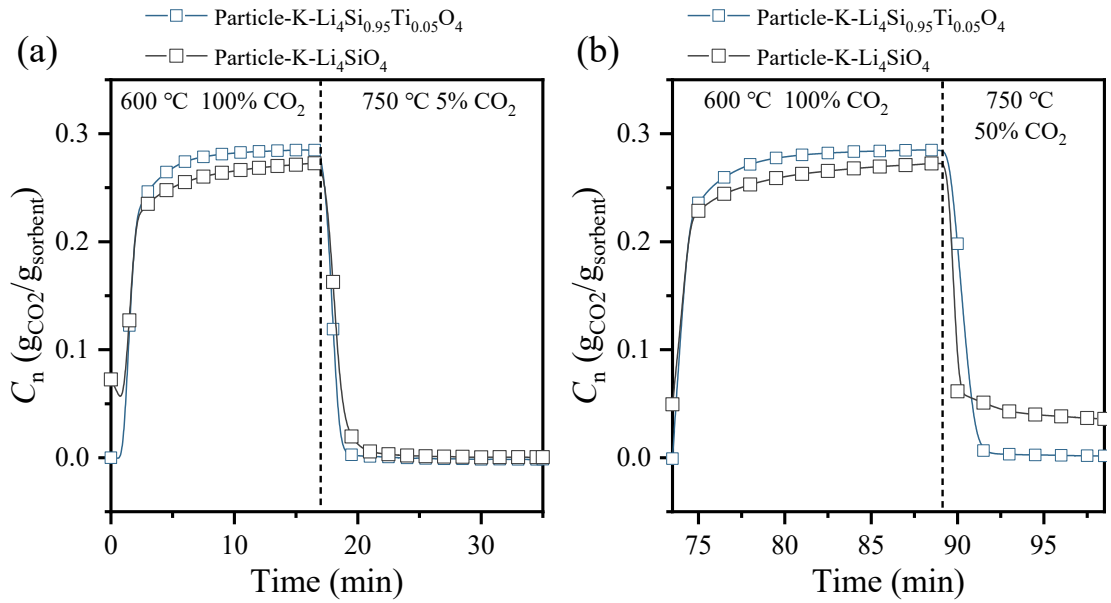

Fig. S10 Thermogravimetric curves of K-$Li_4Si_{0.95}Ti_{0.05}O_4$ and K-Li_4SiO_4 under different desorption atmospheres. Sorption at 600 °C under 100% CO_2, desorption at 750 °C under varied CO_2 concentrations (5%–50%).

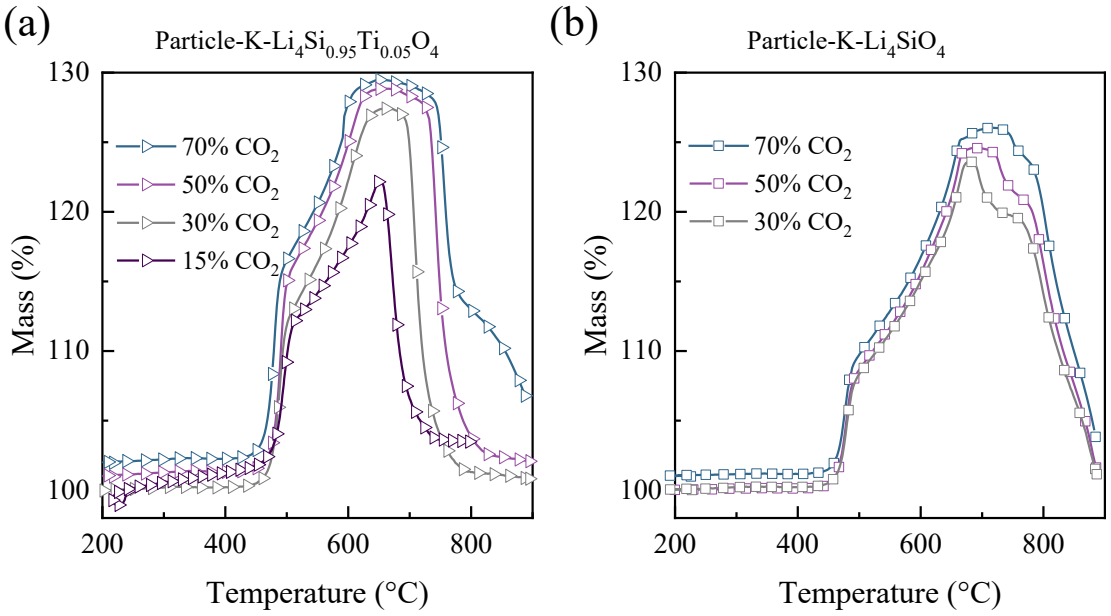

Fig. S11 Dynamic thermogravimetric curves in range of 200–900 °C at a heating rate of 5 °C min^{-1}.

S11 Comparison of CO_2 sorption performance

Table S5 Comparison between literature related to Li_4SiO_4 sorbent and this work (powder morphology)

Note: All data presented in this comparison were obtained using thermogravimetric analysis (TGA).

Chemical composition	Sorbent name	Preparation Method	Exp. Cond.	Capacities in 1st cycle ($g_{CO2}/g_{sorbent}$)	Capacities after cyclic test ($g_{CO2}/g_{sorbent}$)	Ref.
K-Li_4SiO_4 (3wt%K)	LD-P-3K	Impregnation precipitation method	Sorption:100%CO_2,30min, 600 °C; Desorption:100%N_2,15min, 750 °C;	0.261	0.241 (30th cycle)	Yi et al. (2025) [1]
Li_4SiO_4	Li_4SiO_4-4.2 (n(Li/Si)=4.2)	Mechanochemical activation	Sorption:100%CO_2,30min, 700 °C; Desorption:100%N_2,60min, 700 °C;	0.345	0.27 (20th cycle)	Guo et al. (2024) [2]
Li_4SiO_4	Li_4SiO_4-3.2 (n(Li/Si)=3.2)	Mechanochemical activation	Sorption:100%CO_2,30min, 700 °C; Desorption:100%N_2,60min, 700 °C;	0.266	0.25 (20th cycle)	Guo et al. (2024) [2]
(Al, K, Ti, Fe, Ca, Na)-Li_4SiO_4	UPy- Li_4SiO_4 (pyrophyllite as Si source)	Pyrophyllite, liquid phase deposition	Sorption:15%CO_2/N_2,15min, 600 °C; Desorption:100%N_2,15min, 700 °C;	0.249	0.256 (10th cycle)	Cai et al. (2025) [3]

Li_4SiO_4	H200-C800-Li_4SiO_4 (Hydrothermal temperature: 200 °C, calcination temperature:700 °C)	Hydrothermal calcination	Sorption:15%CO_2/N_2,30min, 550 °C; Desorption:100%N_2,10min, 700 °C;	~0.13	0.15 (10^{th} cycle)	Wang et al. (2024) [4]
(K, Na)-Li_4SiO_4	Li_4SiO_4-GC	Solid-state reaction method	Sorption:15%CO_2/N_2,30min, 525 °C; Desorption:100%N_2,10min, 650 °C;	0.28	0.23 (20^{th} cycle)	Tan et al. (2025) [5]
$K_{0.1}Ti_{0.05}$-Li_4SiO_4	K/5TE-PDCs-Li_4SiO_4	Polymer-derived ceramic strategy (PDCs)	Sorption:15%CO_2/N_2,30min, 600 °C; Desorption:100%N_2,10min, 600 °C;	0.241	0.23 (50^{th} cycle)	Cai et al. (2025) [6]
K-Li_4SiO_4	P-3K-1.5M	Dry ball-milling	Sorption:15%CO_2/N_2,40min, 600 °C; Desorption:100%N_2,10min, 700 °C;	0.26	0.23 (10^{th} cycle)	Zhao et al. (2024) [7]
(Al, Fe, Ti)-Li_4SiO_4	LH4.1–500-3 (fly ash as Si source)	Solid-state reaction method	Sorption:100%CO_2,10min, 700 °C; Desorption:100%N_2,10min, 750 °C;	0.332	0.234 (35^{th} cycle)	Mu et al. (2023) [8]
(Ca, Mg, K, Al, Na)-Li_4SiO_4	BR-Li_4SiO_4 (rice husk ash as Si source)	Solid-state reaction method	Sorption:100%CO_2,30min, 675 °C; Desorption:100%N_2,20min, 800 °C;	~0.31	0.28 (30^{th} cycle)	Zhang et al. (2023) [9]
K-Li_4SiO_4	K-Li_4SiO_4	Solid-state reaction method	Sorption: 2000 ppm SO_2, 15% CO_2 and 5 % O_2 balanced by N_2,	~0.13	~0.1 (30^{th} cycle)	Yuan et al.

			20min, 600 °C; Desorption:100%N_2,20min, 700 °C;			(2022)[10]
Li_4SiO_4	Li_4SiO_4	Solid-state reaction method	Sorption:90%CO_2,30min, 600 °C; Desorption:100%N_2,10min, 700 °C;	~0.08	~0.07 (10^{th} cycle)	Yang et al. (2023)[11]
Na-Li_4SiO_4	S9-11-5- Li_4SiO_4	Solution-based method	Sorption: 15% CO_2/N_2, 30min, 625 °C; Desorption:100%N_2,10min, 700 °C;	0.24	0.24(80^{th} cycle)	Ruan et al. (2023)[12]
K-$Li_4Si_{0.95}$ $Ti_{0.05}O_4$	K-$Li_4Si_{0.95}$ $Ti_{0.05}O_4$	Solid-state reaction method	Sorption: 15% CO_2/N_2, 15min, 600 °C; Desorption:100%N_2,15min, 600 °C;	~0.28	0.28 (50^{th} cycle)	This work
K-$Li_4Si_{0.95}$ $Ti_{0.05}O_4$	K-$Li_4Si_{0.95}$ $Ti_{0.05}O_4$	Solid-state reaction method	Sorption: 15% CO_2/N_2, 15min, 550 °C; Desorption:100%N_2,15min, 550 °C;	0.19	0.18 (50^{th} cycle)	This work

Table S6 Comparison between literature related to Li_4SiO_4 sorbent and this work (particle morphology).

Note: † Tested in a fixed-bed reactor; all other studies used TGA.

Chemical composition	Sorbents	Preparation Method	Exp. Cond.	Capacities in	Capacities after cyclic	Compressive	Ref.

				1st cycle ($g_{CO2}/g_{sorbent}$)	test ($g_{CO2}/g_{sorbent}$)	strength	
K-Li_4SiO_4	PL-30K (30wt% K_2CO_3-doped Li_4SiO_4)	Solid-state reaction combined with mechanical press method	Sorption:4%CO_2,45min, 515 °C; Desorption:100%N_2,50min, 660 °C;	~0.25	0.245 (20th cycle)	/	Stefanelli et al. (2025) [13]
K-Li_4SiO_4	K20_I30_s (20wt% K_2CO_3-doped Li_4SiO_4)	Solid-state reaction combined with drip casting method	Sorption:4%CO_2,30min, 580 °C; Desorption:100%N_2,30min, 620 °C;	~0.12	~0.13 (25th cycle)	/	Rossi et al. (2024) [14]
(K, Na)-Li_4SiO_4	LA-WS30/W (30wt% wheat straw-templated Li_4SiO_4)	Sol-gel combined with extrusion-spheronization	Sorption:100%CO_2,30min, 600 °C; Desorption:100%N_2,10min, 750 °C;	~0.17	0.20 (5th cycle)	5.04 MPa	Hu et al. (2023) [15]
Li_4SiO_4	FSC (Freeze-drying Li_4SiO_4 Cylinder)	Freeze-drying method	Sorption:100%CO_2,30min, 710 °C; Desorption:100%N_2,10min, 800 °C;	0.305	~0.30 (40th cycle)	0.43 MPa	Tan et al. (2023) [16]
Li_4SiO_4	OSP (Original Li_4SiO_4	Freeze-drying method	Sorption:100%CO_2,30min, 710 °C; Desorption:100%N_2,10min, 800 °C;	0.209	~0.20 (40th cycle)	37.5 N	Tan et al. (2023) [16]

	Pebbles)						
Li_4SiO_4	Li_4SiO_4 (PIP)	Impregnated suspension combined with polyvinyl alcohol (PVA) method	Sorption:100%CO_2,30min, 600 °C; Desorption:100%N_2,10min, 750 °C;	~0.07	0.28 (30^{th} cycle)	/	Fu et al. (2023) [17]
Li_4SiO_4	LP2.5	Freeze-drying method	Sorption:15%CO_2,30min, 550 °C; Desorption:100%N_2,10min, 700 °C;	0.15	0.168 (10^{th} cycle)	~4N / 10 MPa	Yang et al. (2023) [18]
Li_2CaSiO_4-Li_4SiO_4	LA-20-Ca	Alginate-assisted granulation technique	Sorption:100%CO_2,30min, 600 °C; Desorption:100%N_2,10min, 750 °C;	0.151	0.311 (10^{th} cycle)	/	Hu et al. (2023)[19]
(Al, K, Na, Ca, Fe)-Li_4SiO_4	EP-Li_4SiO_4 (expanded perlite derived Li_4SiO_4)	Solid-state reaction combined with graphite moulding method	Sorption:100%CO_2,30min, 650 °C; Desorption:100%N_2,10min, 800 °C;	~0.225	0.225 (15^{th} cycle)	2.1 MPa	Ni et al. (2021) [20]
K-Li_4SiO_4	PK-LOS (30wt% K_2CO_3-doped Li_4SiO_4)	Solid-state reaction combined with mechanical compression method	Sorption:4%CO_2,6min, 595 °C; Desorption:100%N_2,30min, 660 °C;	~0.05	~0.05 (50^{th} cycle)	/	Stefanelli et al. (2025) [21]
(K, Na)-Li_4SiO_4	LA-RH20 (20 wt% rice husk-templated Li_4SiO_4)	Sol-gel combined with mechanical compression method	Sorption:15%CO_2,30min, 600 °C; Desorption:100%N_2,10min, 750 °C;	~0.13	0.21 (10^{th} cycle)	3.8 N/4MPa	Hu et al. (2021) [22]

K-$Li_4Si_{0.95}Ti_{0.05}O_4$	K-$Li_4Si_{0.95}Ti_{0.05}O_4$ particles	Solid-state reaction combined with extrusion-spheronization method	Sorption: 15% CO_2/N_2, 15min, 600 °C; Desorption: 100%N_2,15min, 600 °C;	~0.27	0.28 (100^{th} cycle)	16.9 N / 9.24 MPa	This work

S12 Thermodynamic equilibrium and theoretical CO_2 removal efficiency

This section investigates the reaction equilibrium of the samples by temperature-programmed CO_2 sorption/desorption. In each test, sorbent particles were heated from room temperature to 900 °C at 5 °C·min^{-1} under atmospheres with different CO_2 partial pressures; the resulting mass-change profiles are shown in Fig. S11. Across all investigated CO_2 partial pressures, the sample mass first increases with temperature and then decreases. At relatively lower temperatures (<500 °C), CO_2 uptake is largely governed by surface/interface reactions, leading to a modest mass gain. With increasing temperature, the growth of Li_2CO_3/Li_2SiO_3 product layers introduces transport resistances (ionic diffusion and gas diffusion through the product shell) that progressively become rate-limiting and sustain further uptake. Upon further heating, thermodynamic equilibrium shifts toward decarbonation; once the desorption rate overtakes the sorption rate, the overall mass declines. The temperature at the peak mass is taken as the apparent sorption-equilibrium temperature under ramped TGA conditions.

$$Li_4SiO_4\ (s) + CO_2(g) \rightleftharpoons Li_2SiO_3(s) + Li_2CO_3(s) \tag{S1}$$

In ramped TGA (Fig. S11), the peak temperature of the mass-gain curve is used as an apparent equilibrium temperature at a given p_{CO2}. Because the peak reflects the condition where the instantaneous sorption and desorption rates are equal under finite heating and transport, it typically overestimates the true thermodynamic equilibrium temperature, especially at low p_{CO2}.

Considering the gas–solid carbonation of Li_4SiO_4 (Eq. S1), the activities of pure solids are taken as unity; the Gibbs free energy change follows Eq. S2.

$$\Delta G = \Delta G^0 + \mathrm{R}T \ln \frac{p_{CO2}}{p^0} \tag{S2}$$

where R=8.314 J mol^{-1} K^{-1} is the universal gas constant, ΔG^0 is the standard Gibbs free energy change, T is the absolute temperature, and p_{CO2} is the CO_2 partial pressure.

At equilibrium, ΔG=0. The equilibrium constant is therefore

$$\mathrm{K_p} = \frac{\mathrm{a}_{Li_2CO_3}\mathrm{a}_{Li_2SiO_3}}{\mathrm{a}_{Li_4SiO_4} p_{CO_2}/p^0} = \frac{p^0}{p_{CO_2,eq}} \tag{S3}$$

The standard Gibbs free energy change can be expressed as Eq. S4

$$\Delta G^0 = \Delta H^0 - T\Delta S^0 \tag{S4}$$

where ΔH^0 and ΔS^0 are the standard reaction enthalpy and entropy changes, respectively.

$$\ln P_{CO2} = \left(\frac{\Delta H^0}{R}\right)\left(\frac{1}{T}\right) - \frac{\Delta S^0}{R} \quad \text{(S5)}$$

$$m = \frac{\Delta H^0}{R}, \quad b = \frac{\Delta S^0}{R} \quad \text{(S6)}$$

$$\ln P_{CO2} = m\frac{1}{T} + b \quad \text{(S7)}$$

According to van't Hoff relation (Eq. S5), linear fitting was performed on the experimentally measured apparent equilibrium sorption temperature data, as shown in Fig. S12.

The values of ΔH^0 and ΔS^0 presented in the table were derived from the slope and intercept of the fitted line (Eqs. S6-7), respectively. The results show a high degree of agreement between the experimental data points and the fitted curve, with R^2>0.96. Furthermore, both ΔH^0 and ΔS^0obtained from the experimental fitting were higher than their corresponding theoretical values (Table S7). The larger $|\Delta H^0|$ yields a steeper slope in the ln $p_{CO2, eq}$-1/T plot (Eq. S7), indicating greater sensitivity of $p_{CO2, eq}$ to temperature at a given p_{CO2}.

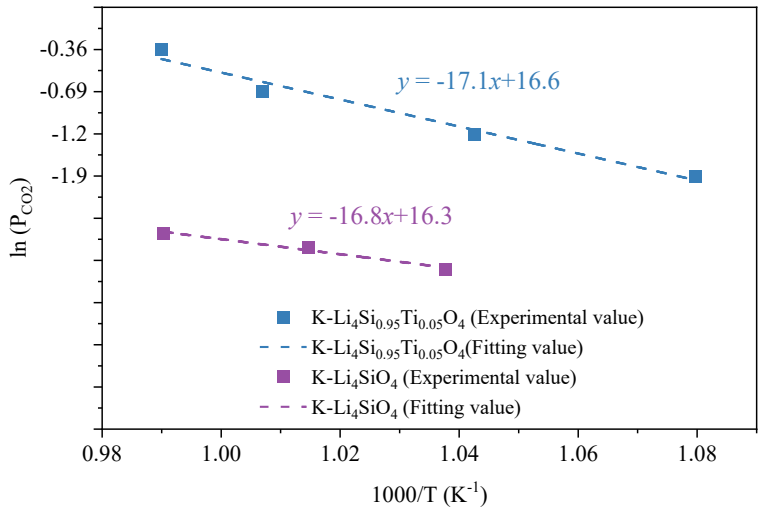

Fig. S12 Linear fitting of the equilibrium CO_2 partial pressures ($p_{CO2, eq}$) obtained from TGA measurements under different inlet CO_2 concentrations. Experimental data points are shown together with the best-fit straight line according to Eq. (S6), from which ΔH^0 and ΔS^0 were extracted.

m (K-$Li_4Si_{0.95}Ti_{0.05}O_4$) = ($\Delta H^0$/R)/1000 = −17.1, b = 16.6

m(K-Li_4SiO_4) = (ΔH^0/R)/1000 = − 16.8, b = 16.3

ΔH^0(K-$Li_4Si_{0.95}Ti_{0.05}O_4$) = m×1000×R = -142.4 kJ mol^{-1}, ΔS^0 (K-$Li_4Si_{0.95}Ti_{0.05}O_4$) = -$b$×R=-138.0 J mol^{-1} K^{-1}

ΔH^0(K-Li_4SiO_4) = m×1000×R = -139.8 kJ mol^{-1}, ΔS^0 (K-Li_4SiO_4) = -b×R = -135.4 J mol^{-1} K^{-1}

Table S7 Fitting results of the thermodynamic parameters at equilibrium state for Li_4SiO_4-based sorbents.

	$\lvert\Delta H^0\rvert$	ΔS^0
Theoretical data (Li_4SiO_4)	119.8	122.8
Experimental data (K-Li_4SiO_4)	139.8	135.4
Experimental data (K-$Li_4Si_{0.95}Ti_{0.05}O_4$)	142.4	138.0

The experimentally determined equilibrium temperatures were compared with predictions from HSC Chemistry 6.0. The results show that the experimental data follow the same trend as the theoretical curves. However, at a given p_{CO2} the experimental equilibrium temperature is consistently higher than the theoretical value. This observation is consistent with prior reports. For example, Zhang et al.[23] reported that K_2CO_3-doped Li_4SiO_4 shows a higher equilibrium temperature than undoped Li_4SiO_4. The fitted lines for K-$Li_4Si_{0.95}Ti_{0.05}O_4$ and K-Li_4SiO_4 particles indicate that Ti doping slightly affects the thermodynamic equilibrium under the conditions studied.

Combining Eqs. S2-S7 yields the relationship between the equilibrium temperature and $p_{CO2,}$ as shown in Eqs. S8-S9.

$$\mathrm{R}T_{\mathrm{eq}} \ln \frac{p_{\mathrm{CO_2}}}{p^{0}} = \Delta S^{0} T_{\mathrm{eq}} - \Delta H^{0} \tag{S8}$$

$$T_{\mathrm{eq}} = \frac{\Delta H^{0}}{\Delta S^{0} - \mathrm{R} \ln p_{\mathrm{CO_2}}} \tag{S9}$$

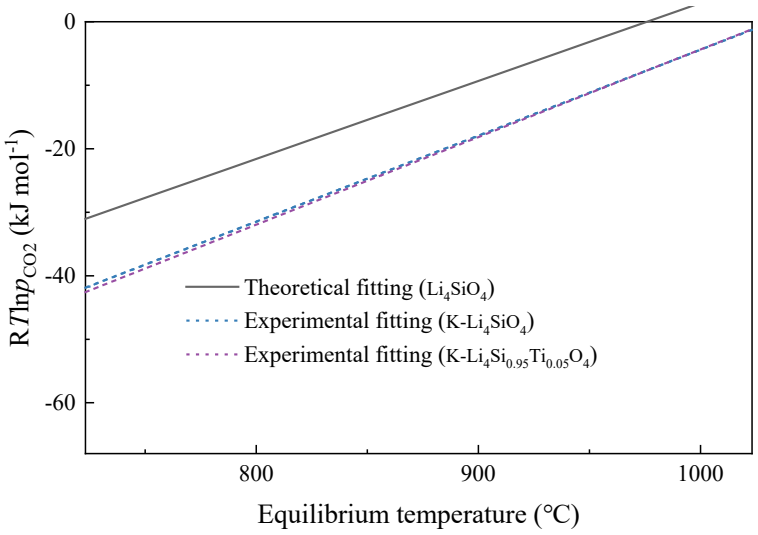

Fig. S13 Comparison between experimental equilibrium CO_2 partial pressures (p_{CO2}) and the theoretical values predicted by thermodynamic calculations. Solid lines represent the calculated curves, while symbols denote the experimental data; the close agreement validates the van't Hoff analysis.

By substituting the fitted ΔH^0 and ΔS^0 into Eq. S6, an empirical formula was established to predict the actual equilibrium CO_2 partial pressures of K-$Li_4Si_{0.95}Ti_{0.05}O_4$ and K-Li_4SiO_4 particles under different sorption temperatures.

$$\ln\ p_{CO2}(\text{K-Li}_4\text{Si}_{0.95}\text{Ti}_{0.05}\text{O}_4) = -\frac{1.7\times10^4}{T} + 16.6; \quad \ln\ p_{CO2}(\text{K-Li}_4\text{SiO}_4) = -\frac{1.7\times10^4}{T} + 16.3 \tag{S10}$$

It can be observed from Eq. S10 that the empirical formulae are virtually identical with and without Ti doping, leading to the conclusion that the doping process does not significantly alter the thermodynamic properties.

For the gas–solid reaction (Eq. S1), activities of pure solids are taken as unity. Using the pressure-form equilibrium constant with standard-state pressure f^0 =1 bar and the ideal-gas approximation ($f_{CO2}\approx p_{CO2}$), we obtain Eq. S11-13. This is consistent with the relations derived in Eqs. S2–S6 and used to convert $p_{CO2,\,eq}$ to K_p in Table S8.

$$K_p \equiv \left(\frac{f_{CO2}}{f^0}\right)^{-1} \Rightarrow K_p = \frac{f_{CO2}}{p_{CO_2,eq}/1bar} \approx \frac{1}{p_{CO_2,eq}} \tag{S11}$$

$$\ln\ K_{CO2}(T) = \frac{\Delta S^0}{R} - \frac{\Delta H^0}{RT} \tag{S12}$$

$$K_p(T) = \exp(K_p(T)), \quad \ln K_p = -\frac{\Delta H^0}{RT} + \frac{\Delta S^0}{R}, \quad \ln p_{CO_2,eq} = \frac{\Delta H^0}{RT} - \frac{\Delta S^0}{R} \tag{S13}$$

$$p_{CO2,eq}(T) = \frac{1}{K_p(T)}(\text{bar}, p^0 = 1\text{bar}) \tag{S14}$$

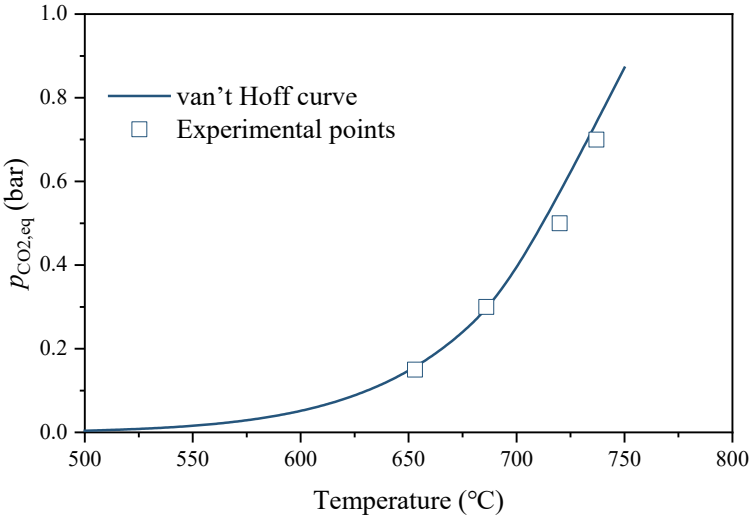

Fig. S14 Nonlinear regression of $p_{CO2,eq}$ versus Temperature for K-$Li_4Si_{0.95}Ti_{0.05}O_4$ particles.

After obtaining $p_{CO2,\,eq}$ (Eq. S14), we computed the thermodynamic upper bound for removal as Eq. S15, and the results are shown in Table S8.

$$\eta_{th} = \max\left(0,\ 1-\frac{p_{CO_2,eq}}{p_{in}}\right) \tag{S15}$$

Note: The calculated η_{th} in Eq. S15 and Table S8 represents the thermodynamic upper limit of CO_2 removal efficiency, obtained under equilibrium conditions while neglecting kinetic and mass transfer limitations.

Table S8. Theoretical CO_2 removal efficiency at different temperatures.

Temperature (°C)	K_p	$P_{CO2,eq}$ (bar)	η_{th} at 15 % CO_2（P_{in}=0.15 bar）
500	256.8	3.9×10^{-3}	97.4 %
550	66.9	1.5×10^{-2}	90.1 %
600	20.3	4.9×10^{-2}	67.2 %

”

S13 Kinetic analysis of CO_2 sorption using a dual-exponential model

To gain deeper insight into the kinetic enhancement induced by Ti doping, the CO_2 sorption profiles of both pristine and Ti-doped Li_4SiO_4 were fitted using a dual-exponential decay model. This empirical model is well-suited for decoupling complex gas-solid reaction processes, typically distinguishing an initial rapid stage (often governed by surface reaction kinetics and/or external diffusion) from a subsequent slower stage (often controlled by solid-state ion diffusion through the product layer). The model is expressed as Eq. S16.

$$y = \mathrm{A}e^{-\mathrm{k}_1 t} + \mathrm{B}e^{-\mathrm{k}_2 t} + \mathrm{C} \tag{S16}$$

$$W_{ad} = \frac{m_{\mathrm{t}}}{m_{\mathrm{t0}}} \times 100\% \tag{S17}$$

where，y represents the normalized mass change percentage (W_{ad}) of the sorbent before and after reaction, calculated according to Eq. S17，m_{t0} and m_t denote the mass of the sorbent at the initial moment and at time t, respectively；t is the reaction time，k_1 and k_2 are the exponential constants representing the rate constants for the initial surface-controlled stage and the subsequent diffusion-controlled stage, respectively; A and B are the pre-exponential factors, and C is a constant intercept.

The fitting results (Table S9 and Fig. S15) reveal that Ti doping enhances both k_1 and k_2 across all temperatures and CO_2 concentrations tested. The concomitant increase in both constants suggests that Ti incorporation impacts multiple processes: the improvement in k_1 likely relates to more efficient surface reaction sites and/or improved CO_2 access, while the more significant enhancement in k_2 provides strong evidence for accelerated bulk ionic mobility (Li^+ and O^{2-} diffusion), which is frequently the rate-limiting step in such solid-state reactions. This is consistent with the hypothesis that Ti-induced lattice distortions create favorable pathways for ion migration.

To quantitatively investigate the influence of different CO_2 concentrations on the reaction behavior of the particles, the activation energy (E_a) for the processes characterized by k_1 and k_2 was estimated for each sample using the Arrhenius equation (Eq. S18):

$$\mathrm{k} = \mathrm{k}_0 \, \mathrm{e}^{\left(-\frac{\mathrm{E}}{\mathrm{R_g T_{ad}}}\right)} \tag{S18}$$

where，k_0 is the pre-exponential factor, E_a represents the apparent activation energy for the surface reaction or diffusion process, R_g denotes the universal gas constant (8.314 $J \cdot mol^{-1} \cdot K^{-1}$), T is the absolute temperature.

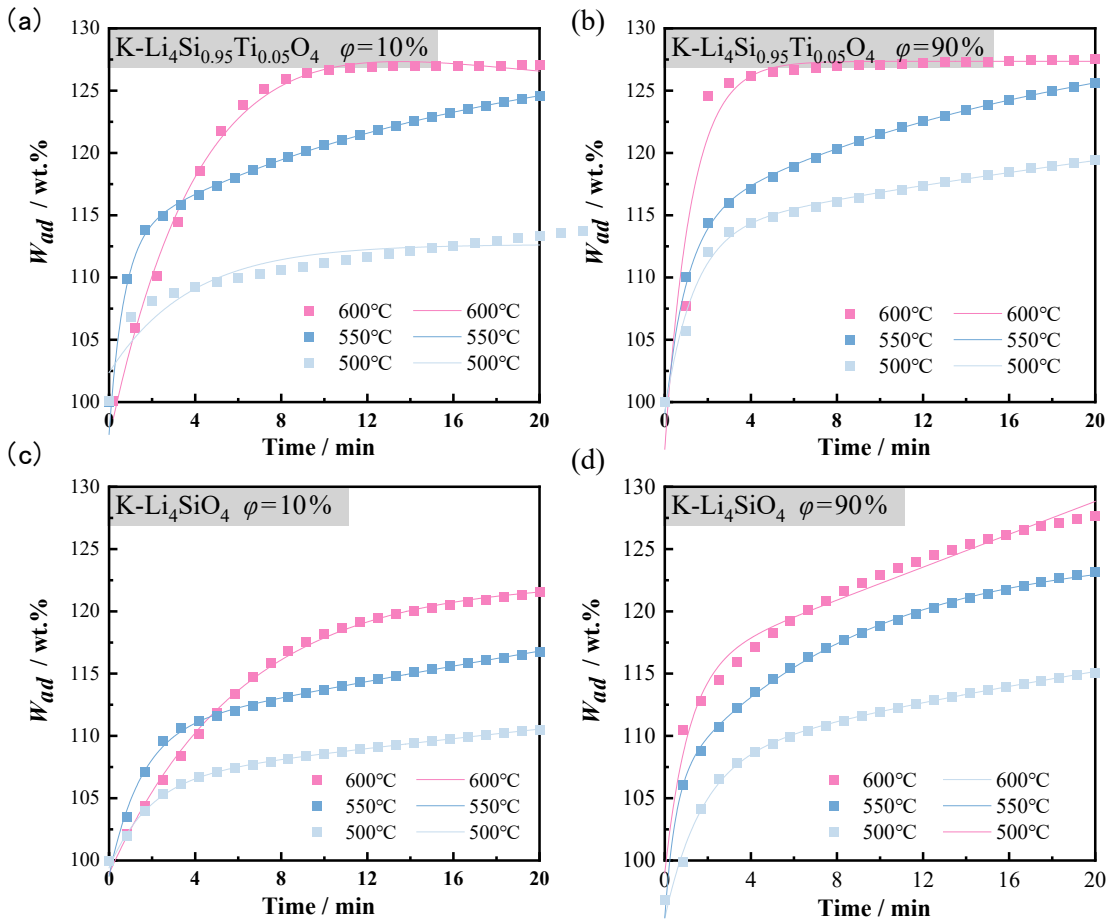

Fig. S15 Dual-exponential model fitting curves of the two sorbent particles under different CO_2 partial pressures.

Table S9 Kinetic parameters derived from the dual-exponential model for the two sorbent particles under various CO_2 partial pressures.

Sample	CO_2 concentrations	Temperature °C	k_1 s^{-1}	k_2 s^{-1}	R^2
K-Li_4SiO_4 particle	10%	600	1.0	0.18	0.95
		550	0.7	0.13	0.99
		500	0.4	0.08	0.99
	90%	600	2.0	0.11	0.95
		550	1.8	0.09	0.99
		500	1.5	0.07	0.97
K-$Li_4Si_{0.95}$ $Ti_{0.05}O_4$ particle	10%	600	1.2	0.20	0.99
		550	0.9	0.14	0.99
		500	0.5	0.09	0.99
	90%	600	2.2	0.13	0.95
		550	2.0	0.10	0.99
		500	1.7	0.08	0.97

S14 Comparison of strength between this work and commercial zeolite catalysts

Table S10. Comparison of crushing/compression strength between this work and commercial zeolite catalysts

Material	Form & Size	Strength	Reference
K-$Li_4Si_{0.95}$ $Ti_{0.05}O_4$ particles	Spheres, 1–1.5 mm	16.9 N (13.7 MPa)	This study
Zeolite particles	Small, ~1.5 mm	~2.3 N (~2.5 MPa)	[24]
Zeolite particles	With binder, ~3 mm	~110 N	[25]
Zeolite extrudates (various diameters)	Ø 10-32 mm	8.8–27.5 MPa	[26]
Zeolite monoliths	Bulk	1.0–1.4 MPa	[27]

Note: Strength is reported either as single-particle crushing strength (N) or bulk compressive strength (MPa), as available in the cited literature. The values for monolithic and composite samples are typically given as compressive strength only; particle-level crushing strength is not applicable (N/A).

S15 Long-term stability of K-$Li_4Si_{0.95}Ti_{0.05}O_4$ particle

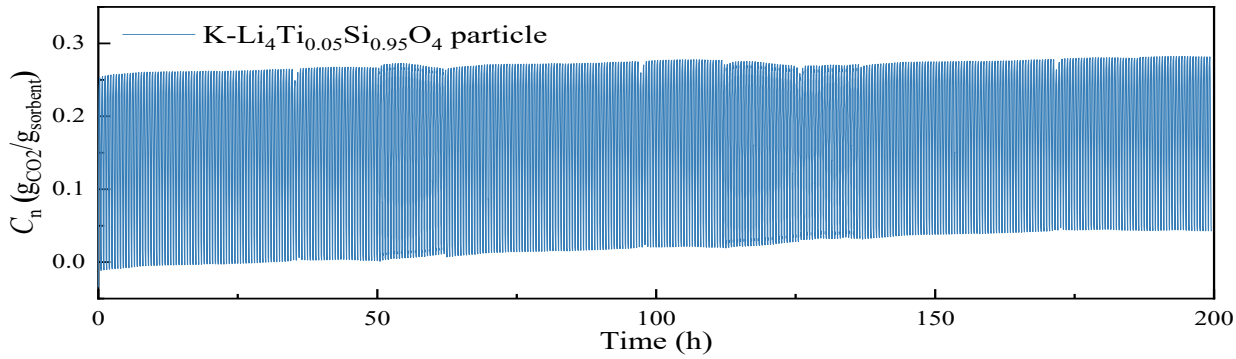

Fig. S16 Long-term stability and cyclability of the K-$Li_4Si_{0.95}Ti_{0.05}O_4$ particle over 400 cycles (equivalent to 200 hours) of CO_2 sorption-desorption (sorption at 600 °C in 15% CO_2 for 15min, desorption at 600 °C in 100% N_2 for 15min).

References

1 J. Yi, R. Fu, Y. Wei and Y. Hu, *Separation and Purification Technology*, 2025, **354**, 129050.
2 A. Guo, L. Huang, C. Cao, Y. Sun, Q. Wang and F. Yu, *Chemical Engineering Journal*, 2024, **485**, 149943.
3 L. Cai, X. Yang, H. Xue and Y. Zhang, *Chemical Engineering Journal*, 2025, **507**, 160674.
4 X. Wang, W. Xia, X. Sun, Y. Yang, X. Ren and Y. Li, *Carbon Capture Science & Technology*, 2024, **13**, 100303.
5 Y. Tan, X. Zhang, W. Wei, W. Hu, H. Xing, S. Wang and W. Liu, *Separation and Purification Technology*, 2025, **353**, 128605.
6 L. Cai, H. Xue, X. Yang, Y. Lin, X. Hu and Y. Zhang, *Chemical Engineering Journal*, 2024, **493**, 152399.
7 P. Zhao, K. Wang, J. Hong and E. J. Anthony, *Carbon Capture Science & Technology*, 2024, **13**, 100255.
8 Y. Mu, T. Wang, M. Zhang and M. Guo, *Fuel Processing Technology*, 2023, **239**, 107533.
9 C. Zhang, C. Li, W. Li and X. Guo, *Separation and Purification Technology*, 2023, **326**, 124730.
10 W. Yuan, T. Deng, S. Chen, Y. He and C. Qin, *Carbon Capture Science & Technology*, 2022, **3**, 100046.
11 Y. Yang, P. Dai, Z. Chen, X. Sun and X. Ren, *Chemical Engineering Journal*, 2023, **468**, 143679.
12 J. Ruan, Y. Tong, J. Ran and C. Qin, *ACS Sustainable Chem. Eng.*, 2023, **11**, 14158–14166.
13 E. Stefanelli, F. Francalanci, S. Vitolo, S. De Santis and M. Puccini, *Journal of Environmental Chemical Engineering*, 2025, **13**, 116102.
14 D. Rossi, I. Anguillesi, U. Desideri and M. Seggiani, *Chemical Engineering Journal*, 2024, **481**, 148615.
15 Y. Hu, H. Lu, Z. Lv, M. Zhang and G. Yu, *Science of The Total Environment*, 2023, **856**, 159275.
16 G. Tan, L. Cai, H. Xue, X. Hu, X. Dong, H. Jiang, X. Yang, Y. Oya and Y. Zhang, *Separation and Purification Technology*, 2023, **311**, 123343.
17 R. Fu, G. Yu, J. Cheng, Y. Hu and S. Yan, *Fuel*, 2023, **331**, 125873.
18 Y. Yang, Z. Zhang, Z. Chen, X. Sun, D. Wu, X. Zhang and W. Liu, *Chemical Engineering Journal*, 2023, **462**, 142297.
19 R. Fu, Y. Hu and W. Wang, *Chemical Engineering Journal*, 2023, **477**, 147156.
20 S. Ni, N. Wang, X. Guo and J. Liu, *Chemical Engineering Journal*, 2021, **410**, 128357.
21 E. Stefanelli, F. Francalanci, S. Vitolo and M. Puccini, *Fuel*, 2025, **380**, 133161.
22 Y. Hu, H. Lu and H. Li, *Ceramics International*, 2021, **47**, 32060–32067.
23 S. Zhang, Q. Zhang, C. Shen, Y. Ni, Y. Wu, Q. Wu and Z. Zhu, *Ind. Eng. Chem. Res.*, 2015, **54**, 7292–7300.
24 E. David, *Archives of Materials Science and Engineering*.
25 A. M. Najafi, S. Soltanali, F. Khorashe and H. Ghassabzadeh, *Chemosphere*, 2023, **324**, 138275.
26 R. Bingre, B. Louis and P. Nguyen, *Catalysts*, 2018, **8**, 163.
27 B. Besser, L. Häuser, L. Butzke, S. Kroll and K. Rezwan, *ACS Omega*, 2017, **2**, 6337–6348.